UNIVERSITY of CALIFORNIA
SANTA CRUZ

IRIS: AN INTENSE RADIATION INTEGRATION SENSOR FOR TERRESTRIAL GAMMA-RAY FLASHES

A thesis submitted in partial satisfaction of the
requirements for the degree of

BACHELOR OF SCIENCE

in

PHYSICS (ASTROPHYSICS)

by

Sophia Urizar

07 June 2024

The thesis of Sophia Urizar is approved by:

Professor David Smith
Advisor

Professor Bruce Schumm
Chair, Department of Physics

Abstract

IRIS: An Intense Radiation Integration Sensor for Terrestrial Gamma-Ray Flashes

by

Sophia Urizar

Terrestrial Gamma-ray flashes (TGFs) are energetic flashes of gamma-rays produced by lightning in thunderstorms. The levels of radioactivity and effects that TGFs have on people and aircraft in close proximity to lightning are still unknown. Current TGF detectors have proven to paralyze and oversaturate when in close proximity to bright TGFs. Because of this, the Intense Radiation Integration Sensor (IRIS) was developed to detect TGFs at close range without saturation, using two photodiodes (bare and with scintillator attached) to detect incoming relativistic Compton electrons from the bremsstrahlung TGF gamma-rays. IRIS was developed at the Santa Cruz Institute of Particle Physics (SCIPP) in Santa Cruz, California and field tested using a Mobetron electron-beam accelerator at the MD Anderson Cancer Center in Houston, Texas. Field testing showed IRIS's sensitivity levels to be higher than we ultimately wanted, warranting next steps in IRIS development to use four bare photodiodes with widely spaced sensistivity levels. Long term IRIS goals include mass production of these dosimeters and distribution to people and aircraft in high lightning areas, using citizen science to help advance the understanding of the radioactivity of TGFs.

Contents

To my parents,

Lara and Lorenzo Urizar,

who taught me the importance of pursuing education.

Acknowledgements

I want to thank Professor David Smith for his endless support and guidance, as well as the rest of the IRIS team: Ronaldo Rodriguez, Michelle Pichardo Munoz, and Heather Mentzer. I would also like to thank the Santa Cruz Institute for Particle Physics (SCIPP) and Dr. Emil Schueler at MD Anderson Cancer Center.

1

Introduction

The Intense Radiation Integration Sensor (IRIS) is an insensitive dosimeter designed to detect terrestrial gamma-ray flashes (TGFs) from a close range, as opposed to current long range detectors. IRIS's main purpose is to research the radiation dosage produced by TGFs, at a close range, and determine the potential harm. IRIS's cost effective design allows for a future of large scale reproduction in order to distribute the dosimeter for citizen science projects concerning TGFs possible hazardous radiation levels.

1.1 Background on TGFs

The newfound phenomena of atmospheric gamma-ray emission, known as terrestrial gamma ray flashes, was first discovered by scintillation detectors aboard the Compton Gamma Ray Observatory (CRGO) spacecraft in 1994 [1]. Because of the

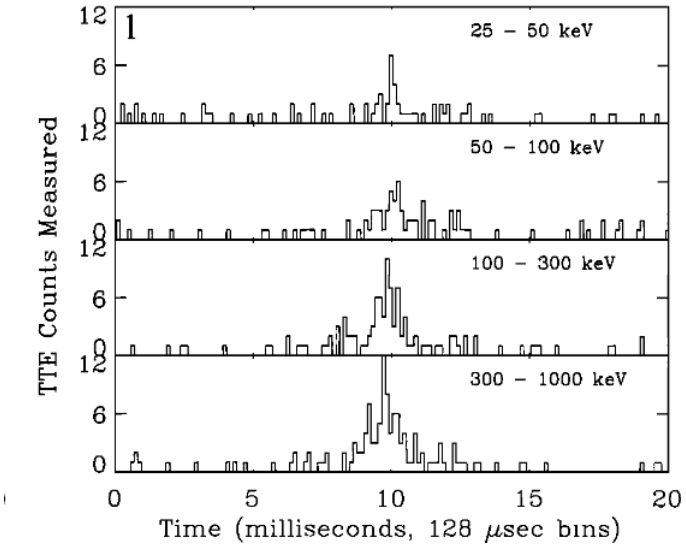

Figure 1.1: BATSE TGF light curve, displaying the duration of the flash and the energy range of the counts plotted [2].

still semi-fledgling understanding of these flashes, the possible radiation hazards of bright and close-range TGFs to people and aircraft are still undetermined. In order to determine the true radiation dosage of these flashes, a device able to withstand close-range flashes without saturating is needed. High dynamic range is a cornerstone of IRIS: a dosimeter with a wide range of gamma-ray detection capabilities to help avoid paralysis and over-saturation.

TGFs are detected in three different methods of observation: ground, aircraft, and spacecraft. These flashes were first characterized by analyzing the Burst and Transient Source Experiment (BATSE) light curves aboard CRGO [2]. An example of a TGF light curve, plotted in four different energy bands, is shown in Figure 1.1. In 2005, another spacecraft named the Reuven Ramaty High Energy Solar Spectroscopic Imager (RHESSI) determined TGFs gamma-ray spectrum to be up to 20 MeV,

well beyond the range detectable by BATSE [3]. RHESSI data also determined the source altitude of TGFs to be less than 30 km via detailed study of their energy spectra [4] and radio observations of the associated lightning [5]. TGF data from the Fermi Gamma-ray Space Telescope refined the time scale of these flashes (via Monte Carlo simulations) to about 10-100 microseconds [6]. Further space based TGF observations, via the Atmosphere-Space Interactions Monitor (ASIM), provided detailed recordings of smaller time scale TGF pulses, due to ASIM's heightened sensitivity [7].

Ground based observations of TGFs provide another batch of data from which the understanding of the atmospheric phenomena has evolved. A TGF produced by rocket-triggered lighting at the International Center for Lightning Research and Testing (ICLRT) in Camp Blanding, Florida, was the first ground-based observation of the phenomenon [8]. In 2009, the first natural cloud-to-ground (CG) associated TGF was observed at ICLRT by the Thunderstorm Energetic Radiation Array (TERA), with an energy spectrum consistent with relativistic runaway electron avalanche (RREA) multiplication [9]. A further confirmation of RREAs being an integral process to TGF formation was confirmed via ICLRT triggered lighting data [10]. The first recorded instance of the production of neutrons from TGFs was by the Gamma ray Observations During Overhead Thunderstorms (GODOT) instrument during a bright, low altitude CG event from an upward positive leader [11]. Ejection of these neutrons, from their nuclei by gamma-rays, left behind clouds of radioactive air [12]. Because of the high intensity of the flash, GODOT was paralyzed, leaving the detection of the neutrons to be the only source of evidence that a TGF took place, illuminating the

need for small scintillation detectors capable of recording such intense flashes without paralysis [13]. More recent ground-based detections of TGFs were recorded 5 km from the detection site in Uchinada, Japan [14], and the first TGF observed from a mountain top was recorded at the Säntis Tower in Switzerland [15].

The first recorded TGF from an aircraft was made by a gamma-ray detector aboard the Airborne Detector for Energetic Lightning Emissions (ADELE) [16]. In 2015, ADELE observed a reverse beam of positrons emitted from TGFs, confirming an already predicted TGF model [17]. The Airborne Lightning Observatory for FEGS and TGFs (ALOFT) detector, aboard a NASA ER-2 aircraft, detected more than 100 TGFs of a variety of durations and peak structures [18].

1.2 Physics behind TGF production

In order to understand TGF production, lighting production must also be understood; TGFs are produced when lightning leaders pass through regions of high electric fields in thunderclouds. Lightning leader initiation begins with the atmospheric ice crystals present in thunderstorms. The ice crystals present are inherently more conductive than air, and therefore act as conductors inside the storm's electric field. The electrons inside of the ice move in response to the direction of the electric field. The direction of the electric field is dependent on the region of the thundercloud, i.e. the positive and negative charge regions, as portrayed in Figure 1.2.

Because of the electric field, the electrons inside the ice crystal are moved and

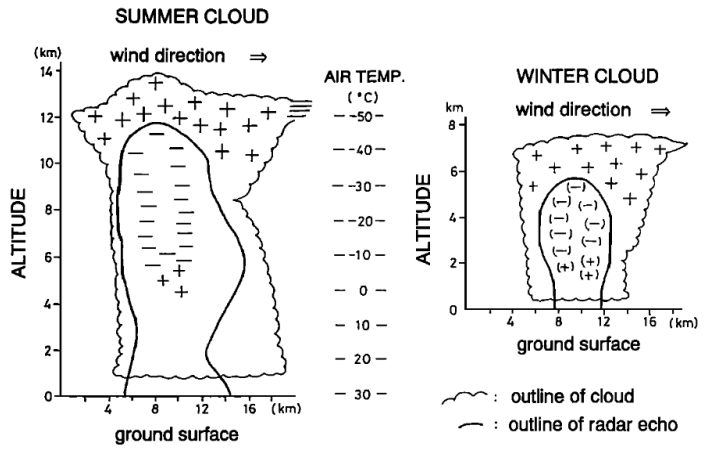

Figure 1.2: Illustration of summer and winter thunderstorms, with negative and positive charge centers labeled [20].

cluster at the tip of the crystal. This congregation of charge at the tip generates an enhanced electric field, ionizing the surrounding air, producing a streamer [19]. This streamer encompasses the conductive ice crystal and the now conductive air ahead of the tip. Streamers can either be positively or negatively charged and move upwards or downwards; the combination of the charge and direction is dependent on the direction of the electric field. When many of these streamers are produced and merge, they become hot and highly conductive. Because they are so highly conductive, the molecules in the streamer ionize the air molecules they collide with; a process which produces a lightning leader [19]. Like streamers, lightning leaders are either positive or negative. Due to the ability to propagate at lower electric field levels, positive streamers are more likely to be produced than negative streamers. Negative leaders are more likely to occur than positive ones. From ice crystals, to streamers, to lightning leaders and then lightning, TGFs are produced.

TGFs can be present in many types of lightning, such as intra-cloud (IC) lightning,

which occurs solely in cloud and never touches ground, CG lightning, and triggered lighting. While it is more likely for lightning, and therefore TGFs, to be caused by negative leaders, it is possible for TGFs to be seen in positive leader lightning [11]. Another factor to account for in TGF and lightning production is the season in which they are produced. In Japan, where previous TGF and lightning studies have been conducted, summer thunderstorms develop at around 6 km (at the bottom of the negative charge region), while winter thunderstorms are present at 2 km [20], as seen in Figure 1.2.

Due to the charged nature of lightning leaders, lightning enhances the electric field surrounding the leader, creating an environment needed for TGF initiation. The electrons in this accelerating electric field, which are integral to the TGF process, must be high-energy and are therefore thought to be secondary cosmic ray electrons [21] or highly-energetic seed electrons ejected from lighting [22]. They are held at non-relativistic speeds due to the friction force between these electrons and the surrounding atmosphere [23], seen in Figure 1.3. When the electric field of the thunderstorm surpasses the 284 kV/m threshold, i.e. the electric field is greater than the friction force on the electron, the electron continues to accelerate and becomes a runaway electron. As seen in Figure 1.3, electrons with an energy level of below 0.3 MeV will slow to a stop, while electrons with higher energies will reach a terminal velocity of 10 MeV.

Because of the high energies of these electrons, when they begin to Møller scatter, a high energy electron-electron elastic scattering process, they create an avalanche

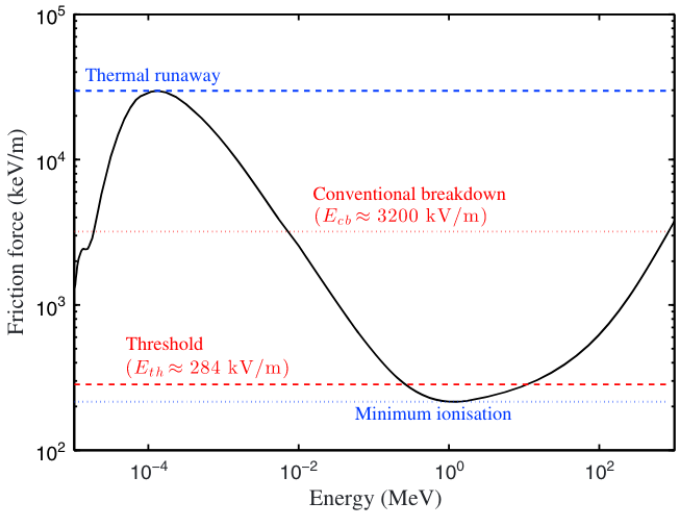

Figure 1.3: The friction force curve of electrons at sea level. The black line represents the friction force on the electron, plotted with respect to the kinetic energy of the electron. The electric field threshold needed for runaway electrons to propagate large distances is about 284 kV/m. The upper limit electric field, which is reached at the tip of the streamer, is about 3200 kV/m [24].

of knock-on electrons, known as the RREA process [25]. These RREA processes were simulated using a Monte Carlo model in order to better understand the electron avalanche rates and direction and velocity of the avalanche propagation [26].

These RREA electrons, through bremsstrahlung interactions with the atmosphere, produce x-rays and gamma-rays [27]. These gamma-rays are what are detected and confirmed when recording TGF data. Figure 1.4 displays the energy of these bremsstrahlung gamma-rays. A secondary effect of these gamma-rays is the production of positrons, via pair production, which propagate in the reverse direction [17]. Gamma-rays with high energies may also produce neutrons via atmospheric photonuclear reactions, leaving behind radioactive air [12].

When the energetic electrons naturally present from cosmic rays undergo the

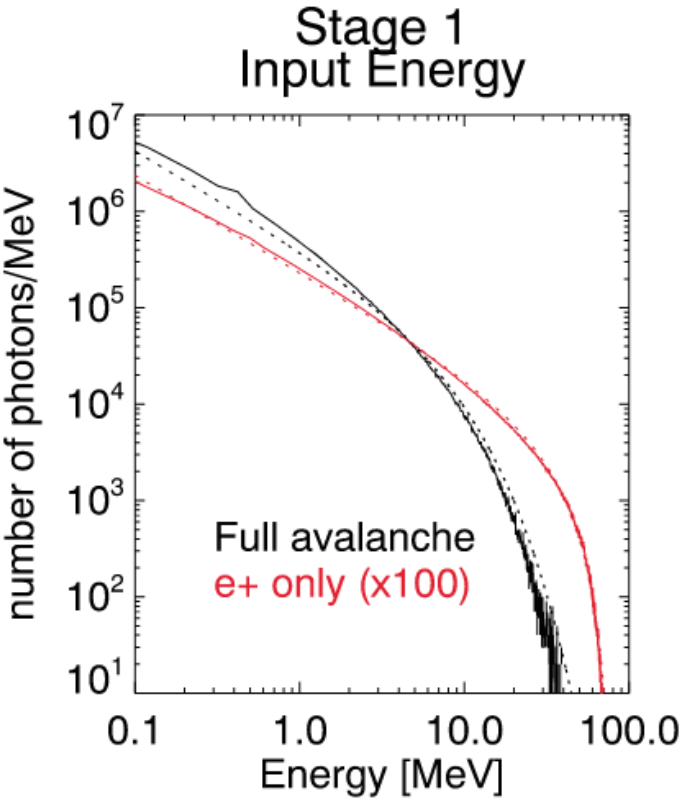

Figure 1.4: The energy of gamma-rays produced by TGF RREA avalanches are seen in black. In red are the gamma-rays produced via bremsstrahlung from the downward positions [17].

runaway electron to RREA process, the reaction produced is both too faint and long a time scale to equate to the brightness and time scale of a TGF. Because the high energy seed electrons needed to begin TGF initiation are too faint in cosmic rays, two mechanisms have been theorized in order to correct this discrepancy.

The two leading TGF production models which account for the high energy electrons needed to produce these flashes are the relativistic feedback model [28] and the lighting leader tip model [22]. The relativistic feedback model supports the theory that there is a fundamental limit of the electric field, and therefore potential differ-

ence, in the electrically charged atmosphere of a thunderstorm [28]. It is believed that each seed electron's ability to avalanche grows with each avalanche generation: each 7 MeV of potential allows 1 seed electron to avalanche into e number of relativistic electrons, on average [8]. This calculation translates into a batch of 100,000 of the RREA electrons creating 1 seed electron, which in turn produces another RREA multiplication process: $\lambda = 1$ is the relativistic feedback parameter used to define this process. Because of the fundamental limit on the potential, when λ is greater than 1, relativistic feedback begins to take place. When λ is greater than 1, the number of avalanches begins to grow exponentially, creating an exponential increase in overall ionization. This heightened ionization then decreases the electric field until λ returns to one. During this process the number of seed elections is increased to a level suitable for TGF production. Figure 1.5 displays the amplification of electrons via the feedback model.

The lightning leader tip model supports the possibility that a high-field region may be created surrounding streamer tips [22]. If this field is high enough a "cold runaway" is possible, meaning each free electron can be accelerated to the high-field region, differing from Dwyer's feedback model. With this possibility, the accelerated free electrons either do not need RREA in order to produce a TGF, or RREA is only present in the cold runaway region, beginning TGF production there.

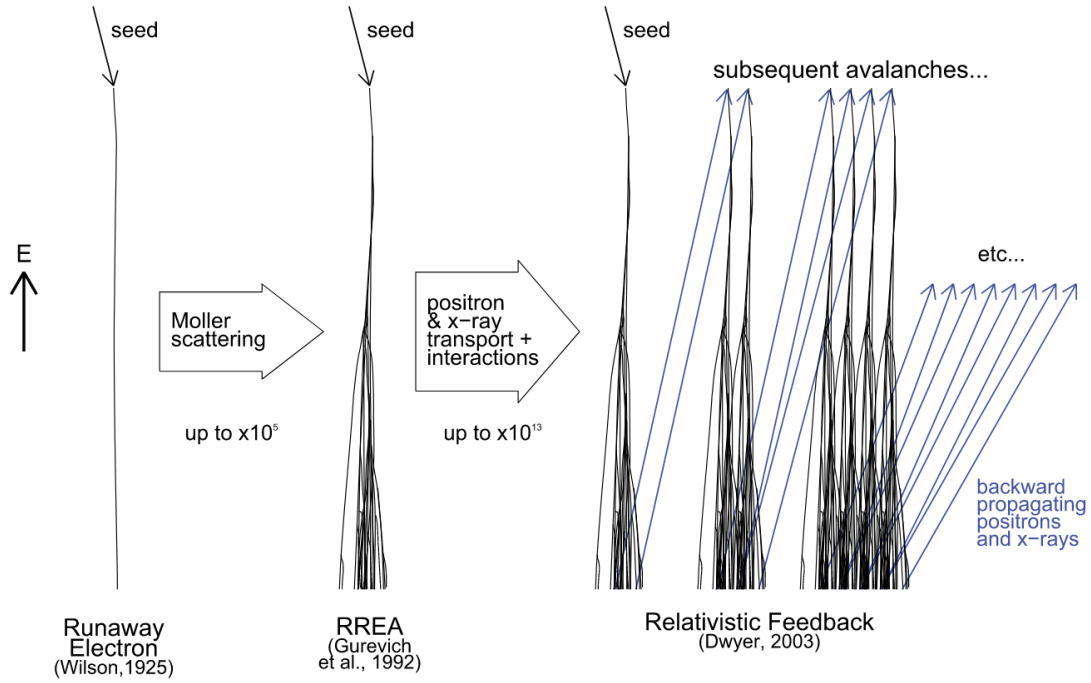

Figure 1.5: The three mechanisms for TGF production: runaway electrons, RREA, Relativistic Feedback. Runaway electrons undergo Møller scattering, producing RREA. With positron production from RREA, the Relativistic Feedback Mechanism is produced. The number of electrons produced in between mechanisms is labeled [29].

1.3 Motivation for IRIS

Although there are spacecraft, aircraft, and ground-based methods of TGF detection, TGFs still saturate detectors during bright flashes. Detectors in space, including BATSE, RHESSI, Fermi, and ASIM, have all been saturated during bright TGF events, creating issues with deadtime (when the processing of one pulse prevents the recording of another) and pileup (recording of incorrect energies due to the close proximity of two pulses in time) [30]. Further evidence of spacecraft TGF saturation is confirmed when comparing TGF count rates from BATSE and RHESSI; bright,

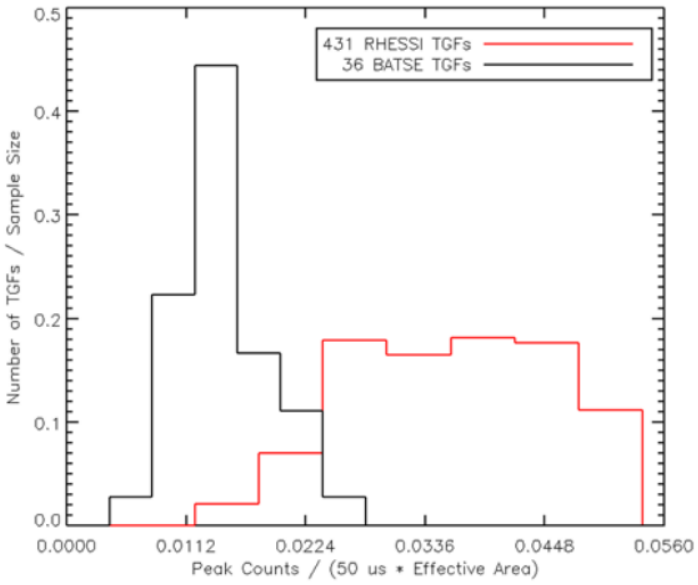

Figure 1.6: Peak count rates for TGFs observed by RHESSI, in red, and BATSE, in black [31].

short, and single-peaked TGFs would not have triggered BATSE, as seen in Figure 1.6. This lack of triggering in BATSE is due to an instrumental deadtime [31]. The ground-based detector GODOT, as stated previously, was also paralyzed by a bright TGF event [13]. In order to properly detect these bright events at a close distance, a smaller, insensitive detector was needed.

IRIS was designed to record TGF data at close range and varying flash brightness's, while also studying the possible radiation risks which TGFs hold. The radiation produced by the runaway electrons, felt by an aircraft in close distance to a TGF, has been estimated to be up to levels as high as 0.1 Sv in less than 1 ms [32]. While this is about the same amount of radiation produced by a full-body CT scan [33], exposure of aircraft to TGFs could pose potential health risks alongside

being hazardous to aircraft avionics [34]. IRIS was designed with detector saturation in mind. With its dynamic range slightly overlapping that of the smallest highest-count-rate scintillator detectors, it extends by roughly 5 orders of magnitude above smaller detector saturation levels.

2

IRIS Design

IRIS will measure TGFs at close range with a large dynamic range of detection in order to avoid saturation. In order to ensure TGF detection, IRIS's lost cost and portable design will allow production and deployment of the dosimeter in great numbers.

2.1 Purpose of IRIS design

IRIS's main purpose is to research the TGF radioactivity levels that may be felt by persons in close proximity to lightning; made possible by IRIS's compact and budget friendly design, allowing mass reproduction of the dosimeter feasible. The close range with respect to TGFs that IRIS will operate allows the PIN photodiodes used on IRIS to be compact and low cost, due to the low voltage needed to run them.

Long term, IRIS will be deployed to high lightning areas, specifically the coastal

part of the Chubu region in the Sea of Japan, where winter thunderstorms produce lightning and TGFs in close proximity to the ground. Another destination for possible deployment is aboard commercial aircrafts, measuring the radioactivity levels which could be affecting the traveling public.

2.2 Detection Method: Photodiodes

When the gamma-rays produced by TGFs interact with the surrounding atmosphere or solid material, they Compton scatter electrons. These relativistic electrons are what IRIS's two OSRAM SFH 2401 silicon PIN photodiodes detect. The photodiode is composed of two doped, or chemically charged, semiconductor p-type and n-type regions. These regions sandwich an undoped intrinsic semiconductor region, as seen in Figure 2.1. The p-type region contains electron holes, while the n-type region contains free moving electrons. When a voltage is applied via battery to the PIN photodiode, and the positive charge region is connected to the n-type and negative to the p-type, the freely moving electrons from the n-type region fill the p-type electron holes. This allows a current to flow from the p to n-type region in a forward bias (reverse bias explained below) in the closed circuit. The intrinsic region, which bleeds into the contact points of the p and n-type regions, is known as the depletion region. When external high-energy electrons (i.e. gamma-rays and photons) pass through this depletion region, the external relativistic electrons excite the diode electrons into the valence band, leaving electron holes behind. The current produced by

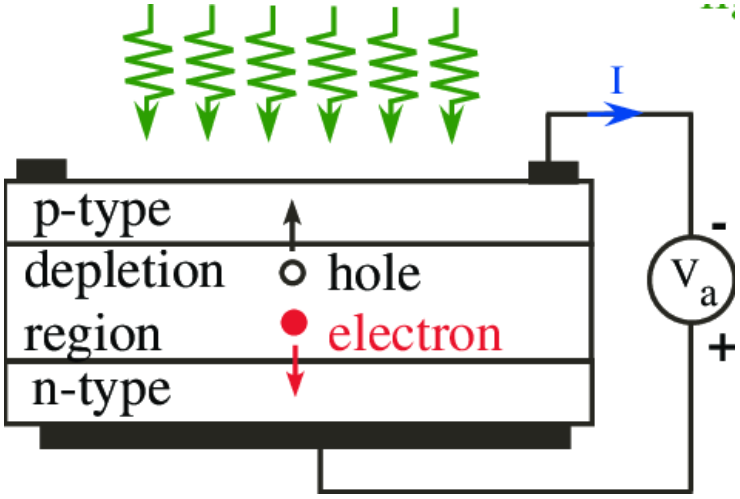

Figure 2.1: Diagram of a PIN photodiode, with labeled p-type, n-type, and depletion regions. Electrons from the n-type region fill the p-type region electron holes [35].

the movement of the electrons and holes in the depletion regions electric field is what is recorded, and the method in which IRIS detects TGFs.

In order to increase the depletion region, or the thickness of the area in which electrons can be detected in the photodiode, a reverse bias is applied to the diode. This bias reverses the direction of the battery, i.e. the placement of positive and negative charge ends (negative end to n-type and positive to p-type). The reversed placement makes the n-type electrons' ability to fill the p-type electron holes more difficult. As a result the direction of the electric field is switched, creating a larger depletion region and allowing a greater area for relativistic electron detection.

In order to achieve a large dynamic range to be able to effectively detect TGFs of various intensities, IRIS's two photodiodes operate at different sensitivity levels. IRIS's photodiodes operate on two separate channels: the bare photodiode channel and the scintillator photodiode channel. The bare diode operates as a reverse bias

PIN photodiode, detecting the Compton scattered electrons from TGFs. The photodiode's depletion region is too small to be able to detect gammas itself, however the scintillator photodiode utilizes a Lutetium Yttrium Orthosilicate (LYSO) scintillator crystal to amplify fainter TGF signals. The LYSO crystal is adhered to the photodiode via optical grease, which is used to lessen internal reflection which the photons undergo at the scintillator/photodiode interface. In addition to the Compton scattered relativistic electrons being directly detected by the photodiode, the scintillator provides a larger area for gamma-rays to penetrate, compared to the photodiodes depletion region alone. This allows both TGF scattered electrons and gamma-rays to be detected. When the TGF gamma-rays pass through the scintillator, they Compton scatter with the electrons present in the LYSO. This excites the electron-hole pairs, which produce photons when the electron-hole pair is re-filled after the initial excitation. Higher energy gammas produce more photons while low energy gammas produce less. These photons are then detected by the depletion region, creating a diode 4 or 5 times, a theorized statistic from IRIS data, more sensitive than the bare channel.

2.3 IRIS Layout

The bare and scintillator photodiode channels are the backbone of the dosimeter's operation. Figure 2.2 displays the printed circuit board (PCB) layout and schematic of the second version of IRIS. When a TGF is detected by IRIS's two photodiodes,

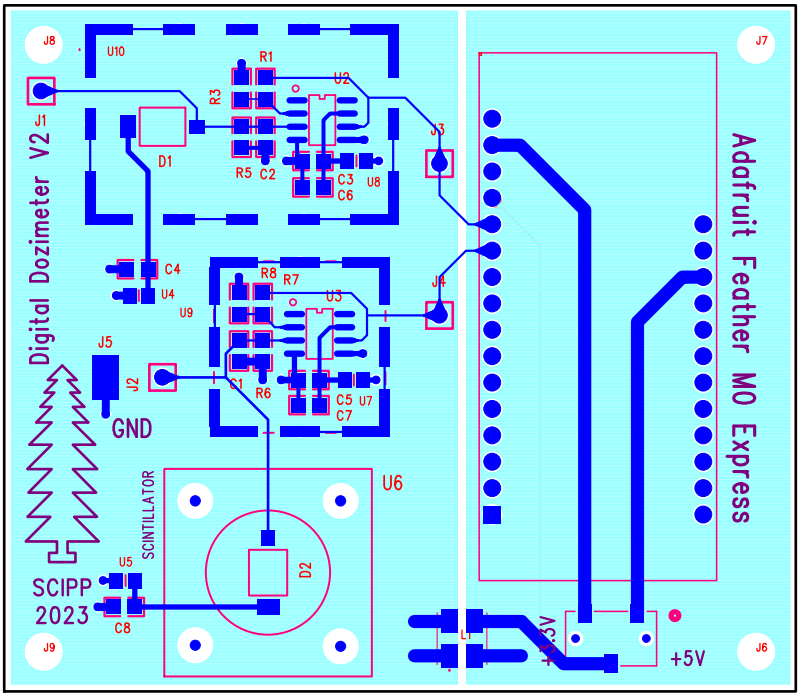

Figure 2.2: The PCB of IRIS V2, with scintillator and bare photodiode channels, as well as Adalogger pin holes.

the charge accumulates on a capacitor that drains through a resistor to ground. Therefore, the voltage across the capacitor has a fast rise and exponential decay, with time constant RC, Eq 2.1 . Each photodiode channel has a corresponding resistor and capacitor with values that determine the RC time constant.

Both the RC time constant,

$$\tau = RC \tag{2.1}$$

and IRIS's output signal (sensitivity), Q referring to charge,

$$V_{signal} = \frac{Q}{C} \tag{2.2}$$

are dependent on the capacitor value used in the respective photodiode channel. Therefore, a change in the photodiode channels capacitor value effects both the re-

spective channels time constant and sensitivity.

When considering time constant values for each channel, particularly referring to high sensitivity from a small capacitance, the baseline voltage, Eq 2.3, is taken into account.

$$V_{background} = IR \tag{2.3}$$

This is due to the time constants impact on resistor values if a small capacitor is in play. The capacitance value must be high enough and therefore the resistor value low enough (see Eq 2.1), to ensure the background signal is not detrimental to signal reading (Eq 2.3), while and the desired time constant and sensitivity are preserved.

The second version (V2) of IRIS has three models with three sets of resistor and capacitor values. The models' different time constant values give IRIS different time scales for TGF pulse recording; the slow, medium, and fast boards have respective slow, medium, and fast time constants on the order of milliseconds. Table 3.1, in Section 3.1, states the resistor, capacitor, and time constant values of each of the V2 models.

For each photodiode channel, the voltage across the resistor and capacitor, produced by the TGF pulse, is fed through an operational amplifier (op amp). The op amp reads the difference across the RC without any current interference due to its infinite impedance. When being read, the voltage is amplified by an approximate gain of 10 due to the op amps two resistors: one to ground and one feedback. The op amp then outputs the 10x gain RC signal.

Figure 2.3 displays the IRIS circuit after photodiode input to the output. The RC

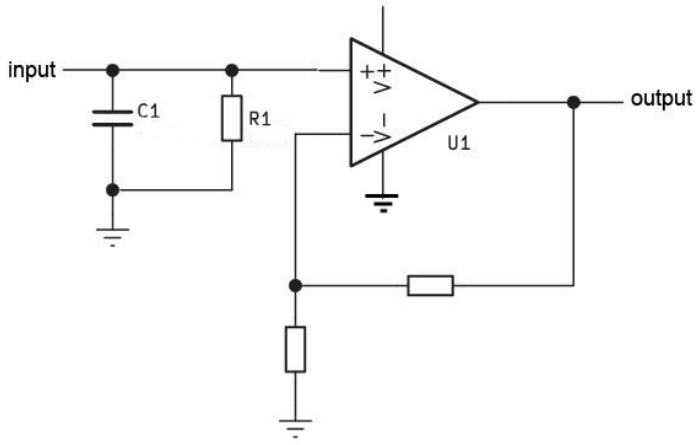

Figure 2.3: The IRIS circuit, displaying the RC, op amp, and feedback resistor. Input is from the photodiode and signal is output to the Adalogger. Image courtesy of Fred Olschner.

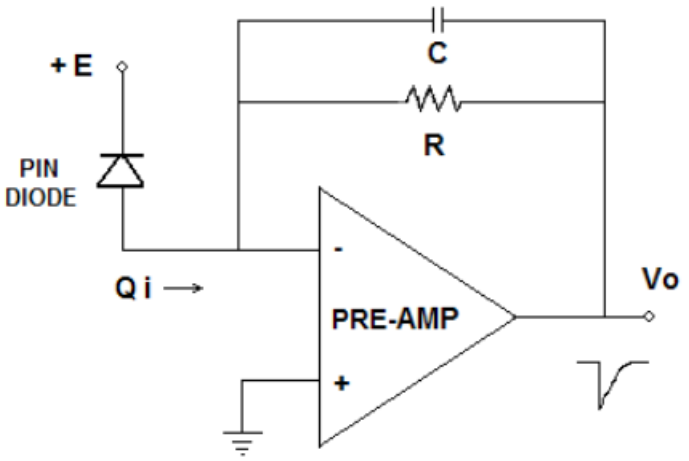

Figure 2.4: PIN photodiode circuit, similar to IRIS, used for X-ray spectroscopy. [36]

resistor and capacitor are labeled as $R1$ and $C1$, which input into the op amp ($U1$). The op amp's feedback resistor is seen, unlabeled, as well as a resistor set to ground. The use of an RC time constant, PIN photodiode, and amplifier by IRIS to detect radiation is a method that has been previously used for X-ray spectroscopy [36], as seen in Figure 2.4.

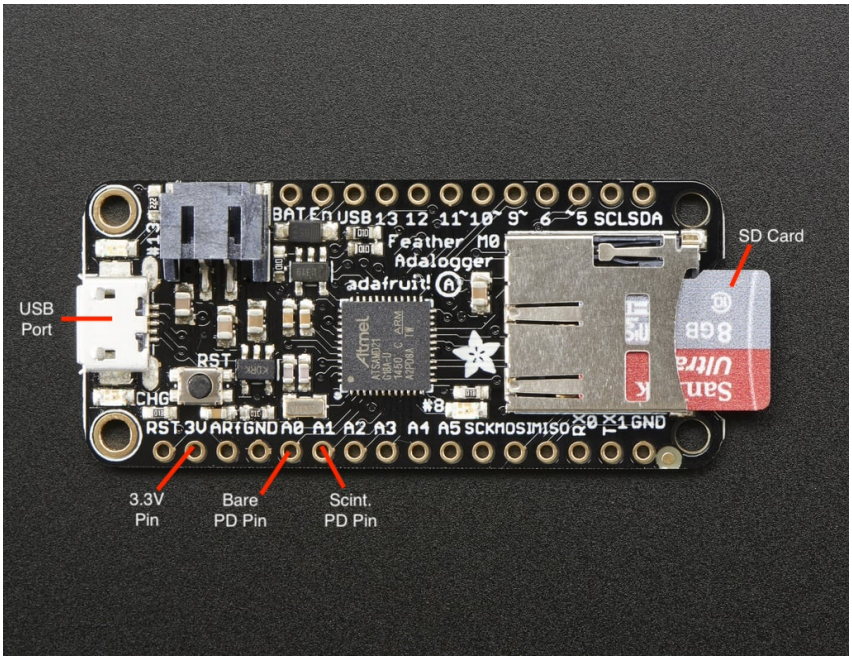

Figure 2.5: Labeled Adalogger with USB port, 3.3 V power pin, bare (A0) and scintillator (A1) pins, and SD card. Background image credit to https://learn.adafruit.com/adafruit-feather-m0-adalogger/overview, accesed on 06/18/2024.

The reverse bias for the photodiodes and the op amps on IRIS are powered via 3.3 V. This 3.3 V either comes from a 3.3 V lithium ion battery (when portable) or through a USB connection. The USB connection is provided by Adafruit's Feather M0 Adalogger. Figure 2.5 displays the Adalogger with labeled pins.

After the TGF signal is output from IRIS's two op amps, it is fed into the Adalogger via connection pins: A0 for the bare photodiode channel and A1 for the scintillator photodiode channel. These voltages are then converted from analog to digital in the Adaloggers built in microcontroller. The 12-bit analog-to-digital converter sums data samples together to reduce noise on the signal, and writes the summed signals onto a SD card connected to the Adalogger. The sampling frequency (50 HZ to 1 kHz) is determined by the specific IRIS models' RC time constant value. After the data is

digitized and summed on the Adalogger, it is fed to a computer via USB. The data transfer from Adalogger to computer is done via Arduino C on the microcontroller side of the serial-over-USB line, and in Python on the computer side of the line. The Arduino IDE interface is the software used in preliminary data viewing and analysis.

Attached to the IRIS PCB are the Aruduino and the LYSO scintillator crystal. The scintillator crystal is held in place with a CNC milled Delrin (thermoplastic) cage. All the IRIS components are attached and kept in a cast aluminum casing, with a connection port to the Arduino for power and data readout. The casing works as a Faraday cage to keep out excess radio frequency (RF) noise. It is tightly sealed to keep out stray light, which would interfere with the data collection by the bare photodiode.

3

IRIS Testing and Data

3.1 Board Characterization

In order to properly understand the TGF pulses which IRIS will detect, the dosimeter underwent in lab pulse characterization tests. Because of the LYSO crystal used on the scintillator photodiode channel, and an inability to reproduce high enough photon counts in our lab to produce a large enough signal, the scintillator crystal was removed for photodiode testing on the three V2 boards. IRIS was tested using the SunLED UV LED to simulate TGF detection in the photodiodes. The board was placed inside a blackout box to ensure no light leakage. The LED was placed horizontally to the bare photodiode (solid angle calculations in Section 3.2).

In order to produce pulses of light with time scales that accurately represented TGFs, a pulser was used. The pulser was connected through a T BNC connector, via BNC cable, to an oscilloscope to view the square wave produced from the LED, for

each testing trail. A secondary BNC was then connected to the oscilloscope, feeding the pulse to the LED via a BNC connector situated on the outside of IRIS's testing box. From the BNC port on the inside of the box, wires were soldered to the LED.

IRIS was powered via 3.3 V from a DC power supply, connected via a direct BNC cable. This cable was then fed to the Adalogger female power pin on the board via a soldered wire pin connection. Depending on which photodiode channel was being tested, the pulses were read out via the Adalogger A0 (bare) or A1 (scintillator) pins via soldered wire pin connection to the BNC port on the box. A BNC cable was then connected to another channel on the oscilloscope to view IRIS's output pulse.

Identical testing procedures were performed for all three V2 models. Errors in the data are approximate: errors in oscilloscope readings are about $\pm$ 1 mV, errors in pulse width readings are about $\pm$ 1 μs. The RC exponential decay of the IRIS pulse was measured and calculated. Due to discontinued production, IRIS used two different packaging models of the OSRAM SFH 2401 silicon PIN photodiode. Table 3.1 displays which V2 boards and channels use either the old discontinued or new photodiode packaging, alongside the resistor and capacitor values used for each channel.

From preliminary tests on measuring the RC time constant, it was found that IRIS's photodiodes contained a stray capacitance. In order to determine the capacitance of the photodiodes, a 2657A High Power System LCR Meter was used. The two photodiode models were soldered to two respective PCBs with SHV ports. The boards were then connected to the meter via SHV cable and the capacitance's were measured: 24 pF for the new packaging and 25 pF for the old packaging. With the

capacitance values of the photodiodes measured, the nominal RC time constants of each V2 board's channels were calculated using Eq 2.1. R refers to the resistor value of the channel and C refers to the sum of the capacitance value of the capacitor and the capacitance value of the respective photodiode model used.

Board	Channel	Resistor ($M\Omega$)	Photodiode C (pF)	Capacitor C (pF)	Nominal τ (ms)	Measured τ (ms)
Slow	A0	200	24	390	82.8	83.5
Slow	A1	200	25	750	155	152
Medium	A0	50	25	150	8.75	9.06
Medium	A1	50	24	200	11.2	12.07
Fast	A0	25	25	25	1.25	1.379
Fast	A1	50	25	25	2.5	2.81

Table 3.1: IRIS V2 Slow, Medium, and Fast board values with respect to bare (A0) and scintillator (A1) channels. Resistor, photodiode capacitance, capacitor capacitance, nominal and measured time constant values are stated.

The measured time constant values for each model's photodiode channels were taken as follows. Each pulse used had a duration less than that of the RC time constant of the channel, but was long enough that the voltage on the capacitor was greater than that of the noise level. These criteria allowed pulses which displayed IRIS's fast rise time and exponential decay on the oscilloscope. The RC time constant was measured using

$$\tau = \frac{ln(V_1) - ln(V_2)}{t} \tag{3.1}$$

with V_1 being a high point on the exponential decay, V_2 being a low point on the decay, and t being the time in between. Table 3.1 displays the measured and nominal time constant values of all three boards six collective channels. Accounting for the 5% error in both resistor and capacitor components, alongside a $\pm$ 1 mV error

when recording values on the oscilloscope, the measured time constant values of the photodiode channels confirmed the calculated nominal values, as expected.

We then characterized IRIS's pulse height in mV vs the LED flashes pulse width. All pulse lengths produced by the pulser are on the scale of μs, in order to accurately resemble TGFs time scales. Because the brightness, i.e. photon count, produced by the LED is a constant value (stated in Section 3.2), the only way to test IRIS's behavior with respect to varying brightness levels was to change the pulse width of the LED flashes. By increasing the pulse width on the pulser of the LED flash, the photodiode on IRIS was exposed to a greater number of photons per flash, and therefore produced a higher output pulse in mV. The behavior is repeated when decreasing the pulse width, producing a lower output pulse height in mV. The behavior, the pulse height with respect to pulse width, of each photodiode channel on the three respective V2 boards can be seen in Tables 3.2, 3.3, 3.4.

V2 Slow

Input Pulse Width (μs)	A0 Output Pulse Height (mV)	A1 Output Pulse Height (mV)
4	189	107
2	96	52
1	44	25
0.8	34	20
0.5	20	12
0.4	15	9.6
0.3	10	6.3
0.2	5	3.22
0.15	3.5	1.7

Table 3.2: V2 Slow pulse data: input pulse width from pulser, output pulse heights from A0 and A1 channels read on oscilloscope.

V2 Medium

Input Pulse Width (μs)	A0 Output Pulse Height (mV)	A1 Output Pulse Height (mV)
25	2790	1910
20	2260	1550
17	1880	1296
15	1680	1132
10	1104	748
7	780	524
5	564	372
2	215	145
1	99.2	67.6
0.5	44	30.6

Table 3.3: As Table 3.2 for V2 Medium pulse data.

V2 Fast

Input Pulse Width (μs)	A0 Output Pulse Height (mV)	A1 Output Pulse Height (mV)
10	3240	3110
5	1810	1570
2.5	868	756
1	340	284
0.75	241	208
0.5	151	127
0.25	56.4	45.2
0.2	40	31.2
0.175	29.6	24.4
0.15	20.2	16.4
0.125	12.8	9.2
0.1	6.2	3.6

Table 3.4: As Table 3.2 for V2 Fast pulse data.

For each board, the pulse heights are seen to increase with increasing pulse width, as expected, confirming the photodiode's ability to create a larger pulse with an increased photon count detection. For each board, each bare photodiode channel's output voltage, with respect input pulse width, is higher than the scintillator photodiodes. This is to be expected because of the bare photodiode channels' lower capacitor values (excluding the Fast board, where the scintillator channel contains a larger resistor value, and capacitor values are equal). The behaviour of a faster time constant producing higher output voltages is also seen when comparing the overall output pulse heights between V2 Fast and V2 Slow. This further confirms that IRIS has an operational RC circuit.

3.2 Power of LED pulse recorded by photodiode

In order to validate our oscilloscopes' measurements of IRIS's output pulse heights, the amount of mW received by the bare photodiode via the LED was calculated. This calculation was done using the LED's spatial distribution curve, seen in Figure 3.1, to calculate the mW per str output by the LED: 1.57. From this, using approximate measurements of the placement of the LED with respect to the bare photodiode (3.3 cm), along with the effective area of the photodiode (7.45 μm^2), the mW received by the photodiode was found to be 1.07×10^{-2}. Converting to mV, accounting for a gain of 10 from the op amp, and assuming a pulse duration of 0.01 ms (capacitance of 25 pF with the calculation done with V2 Fast parameters), the voltage output expected

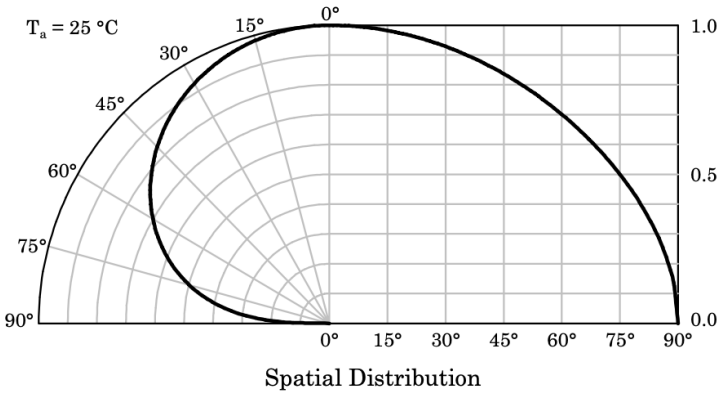

Figure 3.1: Spatial distribution curve of SunLED UV LED. Image courtesy of SunLED UV LED model XZVS54S-9F data sheet, 2021.

from IRIS was calculated to be 4.84 V. Comparing this to the values of 3240 and 3110 mV from Table 3.4, there is room for further analysis due to the discrepancy of the approximate 1 V difference between the calculated and measured values.

3.3 MD Anderson Testing

Field testing for IRIS took place at MD Anderson Cancer Center in Houston, Texas, working alongside Dr. Emil Schueler. TGFs were simulated using a decommissioned Mobetron, an electron-beam linear accelerator, used by Dr. Schueler in his research on radiation cancer therapy. The Mobetron was used to measure IRIS's sensitivity levels with respect to high radiation levels, i.e. high levels of electrons recorded by the photodiodes. The accelerator produced photons at 9 MeV, a high enough energy level to produce bremsstrahlung gamma-rays, allowing the IRIS testing set up to almost accurately mirror what IRIS will detect during deployment (as described in Section 2.3). IRIS was powered via 5 V from a fiber optic receiver box,

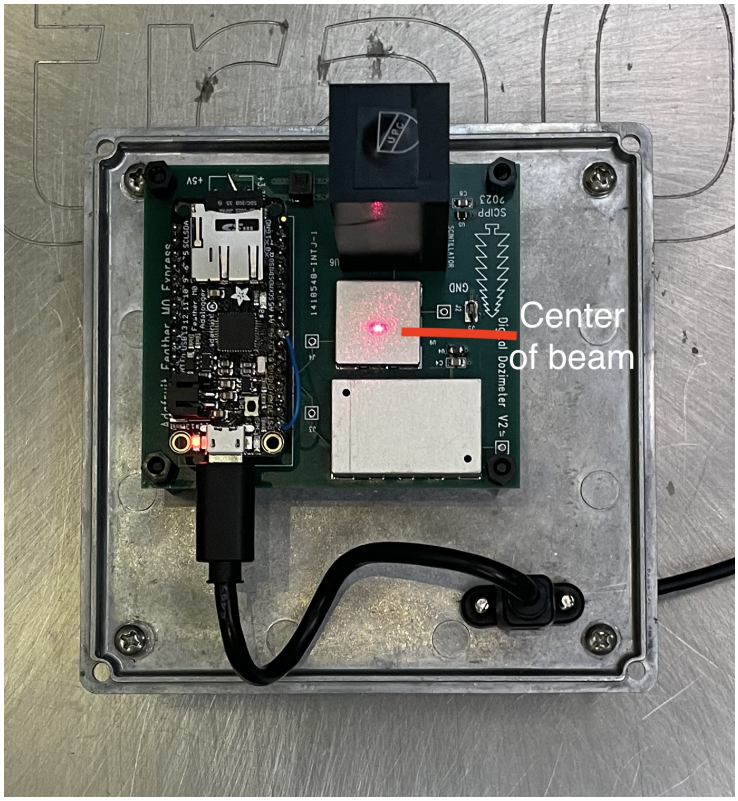

Figure 3.2: Image of IRIS board during testing with labeled position of electron beam.

connected to the Adalogger USB port. The fiber optic cable was connected to a computer, via fiber optic to USB converter, where the IRIS data collected by the Adalogger was read out immediately after recording, and later analyzed via Python and the Arduino IDE interface. Because of high radiation levels, the Mobetron was located in a radiation chamber; testing was done with the chamber door closed and fiber optic cable running underneath the chamber door. IRIS was placed underneath the electron beam, which was centered on the spot between the bare and scintillator photodiodes, seen in Figure 3.2. The beam was broad enough to cover both sensors with a proportional illumination to that of the beam center. All three V2 IRIS models, with slow, medium, and fast time constants, were tested.

Testing began by measuring each of the IRIS baseline levels, IRIS's leakage current rate in an ambient setting with no radiation. Following baseline measurements, IRIS began radiation testing. From preliminary tests on each board, the 9 MeV electron beam proved to saturate each IRIS board and channel. Because of this saturation, attenuators were introduced into the testing setup: Solid Water and lead sheets. Solid Water is a plastic with a density comparable to water that is used in radiotherapy. When the electron beam penetrates the Solid Water, the electrons slow down from relativistic speeds and either completely stop or undergo bremsstrahlung radiation, leaving about 10-30% of the original number of electrons, which have undergone the transition to gamma-rays. When the Solid Water is placed atop IRIS, buffering the electron beam, the bremsstrahlung gamma-rays produced in the Solid Water then pass through IRIS's aluminum casing. 1-3% of these gamma-rays Compton scatter through the passive material above the photodiode, producing the relativistic electrons that IRIS photodiodes detect.

Some testing scenarios solely used Solid Water to attenuate the electron beam, while others used lead sheets in tandem with the Solid Water. The placement of the lead sheets determined the method in which the electron beam was attenuated. When placed above the Solid Water, and beneath the electron beam, a percentage of the incoming electrons undergo bremsstrahlung radiation. Due to the higher atomic number of lead, with respect to plastic, more than 30% of the incoming electrons will undergo bremsstrahlung, producing gamma-rays. Some of those gamma-rays will Compton scatter when entering the Solid Water below. When the lead sheet is

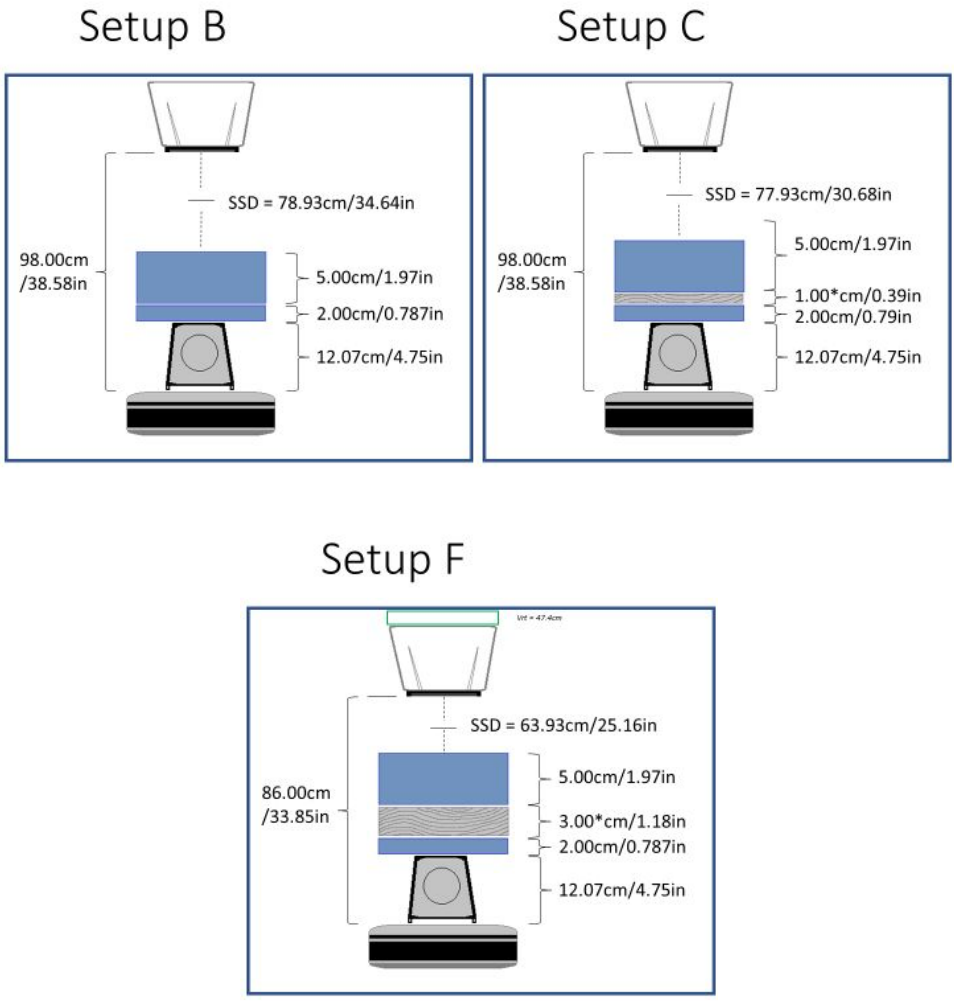

Figure 3.3: Three different IRIS, Solid Water, and lead sheet configurations during testing. Configuration B gives the largest signal, then C, then F. Heights of sheets, Solid Water, and distances between IRIS and beam head are labeled. Image courtesy of Brett Velasquez at MD Anderson Cancer Center.

placed underneath the Solid Water, the out coming gamma-rays from the Solid Water Compton scatter inside of the sheet, or are photoelectrically absorbed if at an energy less than 500 keV. Thus making the placement of the lead sheet underneath the Solid Water a greater attenuator, due to less bremsstrahlung gamma-rays produced and the more photoelectric absorption, than when the sheet is placed above the Solid Water.

Figure 3.3 displays the several different lead sheet and Solid Water configurations used during testing.

The Mobetron was set at a varied pulse width for each trial. The electron beam was either flashed a varied number of times in conventional mode (Conv.), or just pulsed once (FLASH). A select number of tests for the Fast, Medium, and Slow boards, with confirmed attenuation set-ups and time stamps, are stated in Tables 3.5, 3.6, 3.7. A majority of the presented data for the Fast and Medium boards used the conventional mode. The FLASH beam, overall, was too bright for these two boards smaller and more sensitive capacitors. However, the data presented for the Slow board solely used the FLASH pulse type. This is because the time scale of the conventional pulse proved to be smaller than the time scale of the Slow boards decay time. The Slow board does not yet have confirmed data for the A1 channel.

V2 Fast

Run, Channel	Attenuation Set-Up	Pulse Type	Pulse Width (s)	Initial Observed Output (mV)
2110, A0	C	Conv.	1.20e-6	300
2111, A1	C	Conv.	1.20e-6	2800
2113, A0	B	Conv.	1.20e-6	580

Table 3.5: V2 Fast MD Anderson testing data: run number, photodiode channel, Mobetron pulse type and width, initial observed pulse output. The initial observed output was recorded via the Arduino IDE raw data readout before summation of data.

From initial observations of the output pulse height, read out via the Arduino IDE interface, the A0 channel is seen to be less sensitive than the A1 channel, for the selected test runs, as expected. Alongside this, the configurations of attenuation

V2 Medium

Run, Channel	Attenuation Set-Up	Pulse Type	Pulse Width (s)	Initial Observed Output (mV)
2136, A0	F	Flash	5.00e-7	2500
2138, A0	F	Conv.	1.20e-6	110
2139, A1	F	Conv.	1.20e-6	250

Table 3.6: As Table 3.5 for V2 Medium testing data.

V2 Slow

Run, Channel	Attenuation Set-Up	Pulse Type	Pulse Width (s)	Initial Observed Output (mV)
2144, A0	F	Flash	5.00e-7	1600
2160, A0	F	Flash	2.00e-6	3000
2206, A0	F	Flash	5.00e-7	1500

Table 3.7: As Table 3.5 for V2 Slow testing data.

mediums and their sensitivities correlate to the intensity of the output pulse observed in the given data. Both of these observations confirm IRIS's ability to correctly detect relativistic electrons and produce a corresponding pulse height with respect to the given time constant.

Figure 3.4 displays the plotted pulses for the trials 2110, 2139, and 2160 from the respective Fast, Medium, and Slow boards. The conventional setting was used for the Fast and Medium testing runs, while the FLASH setting was used in in the Slow testing run. When viewing the pulse plotted from the slow board, the sharp rise and exponential decay from the IRIS RC time constant is visible.

A detailed analysis of the relationship between IRIS's measured peak voltage and time constant per trial, versus each trials theoretical calculation of the expected values

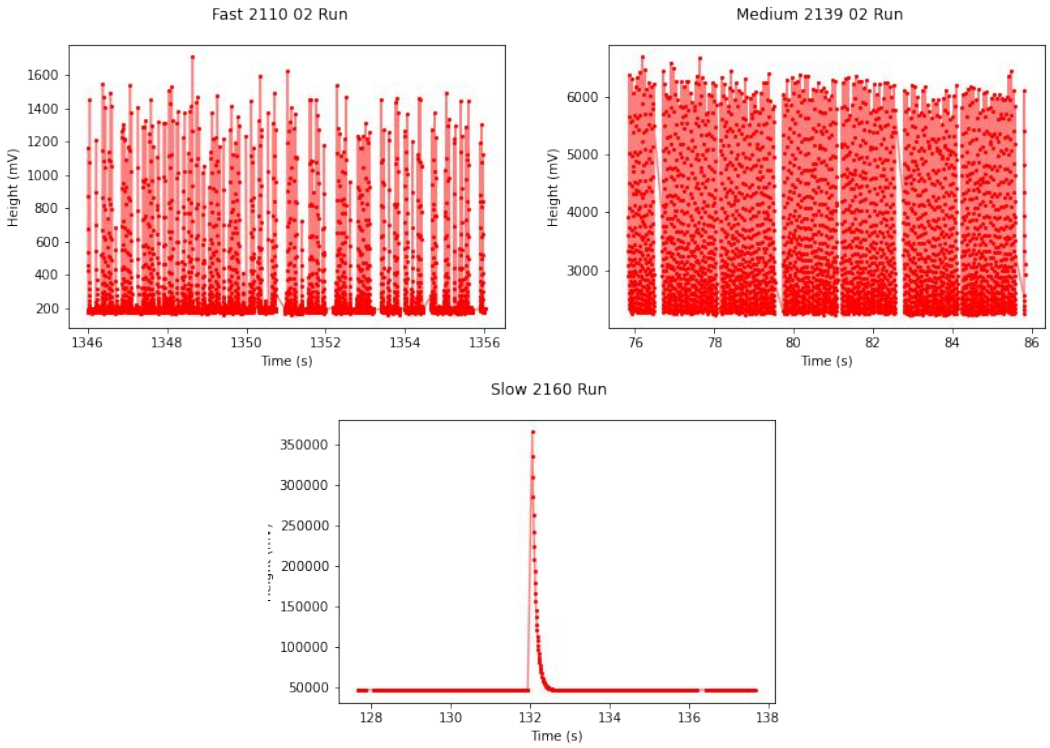

Figure 3.4: Plotted data from Fast, Medium, and Slow board runs at MD Anderson. The header numbers represent the trial and the run; there are up to three runs per trial.

is needed. This analysis will further our understanding of IRIS's operation while continuing to evaluate which capacitance values, and therefore time scale values, to implement in order insure enhanced TGF recording.

From preliminary results, and the necessity of the lead sheet and Solid Water attenuation methods when testing at MD Anderson, IRIS sensitivity levels are determined to be higher than necessary. In order to make IRIS less sensitive and increase the dosimeters dynamic range, a new design of 4 bare photodiode channels has been proposed.

4

Conclusion

The IRIS detector was developed to detect TGFs in short range without saturation in order to study the intensity of the radioactivity produced by these gamma-ray flashes. The detector's two photodiode channels, bare and scintillator, proved to be oversensitive to relativistic electrons when testing at the MD Anderson Cancer Center. Preliminary evaluations of the data show that the current IRIS model studied and developed in these tests, V2, will need modifications in order to detect TGFs without fear of saturation. These future modifications include a four channel photodiode circuit, using only bare photodiodes, in order to keep a large dynamic range with four separate time constants, as well as avoid saturation. Long term, with an evolved IRIS circuit fit for short range TGF detection, the IRIS dosimeter will be mass produced and distributed to people in high lightning areas in order to maximize the data collection of TGF radiation levels and their effects on these people.

Bibliography

[1] G. J. Fishman, P. N. Bhat, R. Mallozzi, J. M. Horack, T. Koshut, C. Kouveliotou, G. N. Pendleton, C. A. Meegan, R. B. Wilson, W. S. Paciesas, S. J. Goodman, and H. J. Christian, Science **264**, 1313–1316 (1994).

[2] R. J. Nemiroff, J. T. Bonnell, and J. P. Norris, Journal of Geophysical Research: Space Physics **102**, 9659–9665 (1997).

[3] D. M. Smith, L. I. Lopez, R. P. Lin, and C. P. Barrington-Leigh, Science **307**, 1085–1088 (2005).

[4] J. R. Dwyer and D. M. Smith, Geophysical Research Letters **32**, 2005GL023848 (2005).

[5] S. A. Cummer, Y. Zhai, W. Hu, D. M. Smith, L. I. Lopez, and M. A. Stanley, Geophysical Research Letters **32**, 2005GL022778 (2005).

[6] G. Fitzpatrick, E. Cramer, S. McBreen, M. S. Briggs, S. Foley, D. Tierney, V. L. Chaplin, V. Connaughton, M. Stanbro, S. Xiong, J. Dwyer, G. J. Fishman, O. J. Roberts, and A. Von Kienlin, Physical Review D **90**, 043008 (2014).

[7] N. Østgaard *et al.*, Journal of Geophysical Research: Atmospheres **124**, 14024 (2019).

[8] J. R. Dwyer, H. K. Rassoul, M. Al-Dayeh, L. Caraway, B. Wright, A. Chrest, M. A. Uman, V. A. Rakov, K. J. Rambo, D. M. Jordan, J. Jerauld, and C. Smyth, Geophysical Research Letters **31**, 2003GL018771 (2004).

[9] J. R. Dwyer, M. M. Schaal, E. Cramer, S. Arabshahi, N. Liu, H. K. Rassoul, J. D. Hill, D. M. Jordan, and M. A. Uman, Journal of Geophysical Research: Space Physics **117**, 2012JA017810 (2012).

[10] B. M. Hare, M. A. Uman, J. R. Dwyer, D. M. Jordan, M. I. Biggerstaff, J. A. Caicedo, F. L. Carvalho, R. A. Wilkes, D. A. Kotovsky, W. R. Gamerota, J. T. Pilkey, T. K. Ngin, R. C. Moore, H. K. Rassoul, S. A. Cummer, J. E. Grove, A. Nag, D. P. Betten, and A. Bozarth, Journal of Geophysical Research: Atmospheres **121**, 6511–6533 (2016).

[11] G. S. Bowers, D. M. Smith, G. F. Martinez-McKinney, M. Kamogawa, S. A. Cummer, J. R. Dwyer, D. Wang, M. Stock, and Z. Kawasaki, Geophysical Research Letters **44**, (2017).

[12] T. Enoto, Y. Wada, Y. Furuta, K. Nakazawa, T. Yuasa, K. Okuda, K. Makishima, M. Sato, Y. Sato, T. Nakano, D. Umemoto, and H. Tsuchiya, Nature **551**, 481–484 (2017).

[13] D. M. Smith, G. S. Bowers, M. Kamogawa, D. Wang, T. Ushio, J. Ortberg,

J. R. Dwyer, and M. Stock, Journal of Geophysical Research: Atmospheres **123**, (2018).

[14] J. Ortberg, D. M. Smith, M. Kamogawa, J. Dwyer, G. Bowers, J. Chaffin, J. Lapierre, D. Wang, T. Wu, and T. Suzuki, Journal of Geophysical Research: Atmospheres **129**, e2023JD039020 (2024).

[15] J. M. Chaffin, D. M. Smith, J. Lapierre, S. Cummer, J. Ortberg, A. Sunjerga, A. Mostajabi, M. Rubinstein, and F. Rachidi, Journal of Geophysical Research: Atmospheres **129**, e2023JD039761 (2024).

[16] D. M. Smith, J. R. Dwyer, B. J. Hazelton, B. W. Grefenstette, G. F. M. Martinez-McKinney, Z. Y. Zhang, A. W. Lowell, N. A. Kelley, M. E. Splitt, S. M. Lazarus, W. Ulrich, M. Schaal, Z. H. Saleh, E. Cramer, H. Rassoul, S. A. Cummer, G. Lu, X.-M. Shao, C. Ho, T. Hamlin, R. J. Blakeslee, and S. Heckman, Journal of Geophysical Research **116**, D20124 (2011).

[17] G. S. Bowers, D. M. Smith, N. A. Kelley, G. F. Martinez-McKinney, S. A. Cummer, J. R. Dwyer, S. Heckman, R. H. Holzworth, F. Marks, P. Reasor, J. Gamache, J. Dunion, T. Richards, and H. K. Rassoul, Journal of Geophysical Research: Atmospheres **123**, 4977–4987 (2018).

[18] M. Marisaldi *et al.*, AGU23 (2023).

[19] Y. P. Raizer, J. Allen, and V. Kisin, (1991).

[20] N. Kitagawa, Journal of Geophysical Research: Atmospheres **99**, 10713–10721 (1994).

[21] A. Gurevich, G. Milikh, and J. Valdivia, Physics Letters A **231**, 402–408 (1997).

[22] G. D. Moss, V. P. Pasko, N. Liu, and G. Veronis, Journal of Geophysical Research: Space Physics **111**, 2005JA011350 (2006).

[23] C. T. R. Wilson, Mathematical Proceedings of the Cambridge Philosophical Society **22**, 534–538 (1925).

[24] A. B. Skeltved, N. Østgaard, B. Carlson, T. Gjesteland, and S. Celestin, Journal of Geophysical Research: Space Physics **119**, 9174–9191 (2014).

[25] L. Babich, I. Kutsyk, E. Donskoy, and A. Kudryavtsev, Physics Letters A **245**, 460–470 (1998).

[26] N. G. Lehtinen, T. F. Bell, and U. S. Inan, Journal of Geophysical Research: Space Physics **104**, 24699–24712 (1999).

[27] J. R. Dwyer, Geophysical Research Letters **30**, 2003GL017781 (2003).

[28] J. R. Dwyer, Journal of Geophysical Research: Atmospheres **113**, 2007JD009248 (2008).

[29] J. R. Dwyer, D. M. Smith, and S. A. Cummer, Space Science Reviews **173**, 133–196 (2012).

[30] D. Sarria, N. Ostgaard, M. Marisaldi, A. Lindanger, A. Mezentsev, N. G. Lehtinen, T. Neubert, F. Christiansen, and R. Victor, in *AGU Fall Meeting Abstracts* (PUBLISHER, ADDRESS, 2021), Vol. 2021, pp. AE14A–05.

[31] B. W. Grefenstette, D. M. Smith, J. R. Dwyer, and G. J. Fishman, Geophysical Research Letters **35**, 2007GL032922 (2008).

[32] J. R. Dwyer, D. M. Smith, M. A. Uman, Z. Saleh, B. Grefenstette, B. Hazelton, and H. K. Rassoul, Journal of Geophysical Research: Atmospheres **115**, 2009JD012039 (2010).

[33] M. Pallu, S. Celestin, F. Trompier, and M. Klerlein, Journal of Geophysical Research: Atmospheres **128**, e2022JD037569 (2023).

[34] M. Tavani, A. Argan, A. Paccagnella, A. Pesoli, F. Palma, S. Gerardin, M. Bagatin, A. Trois, P. Picozza, P. Benvenuti, E. Flamini, M. Marisaldi, C. Pittori, and P. Giommi, Natural Hazards and Earth System Sciences **13**, 1127–1133 (2013).

[35] O. Emile and J. Emile, Energy, linear and angular momentum of light: what do we measure?, 2018.

[36] L. Mondragón-Contreras, F. Ramírez-Jiménez, E. Aguilera-Reyes, and C. Ojeda-Nava, PIN Photo-diodes as Radiation Detectors in Accelerator Applications., 2010.